Journal of Nuclear Materials

Evolution of the oxide structure of 9CrODS steel exposed to supercritical water

Jeremy Bischoff [a,*], Arthur T. Motta [a], Robert J. Comstock [b]

[a] Department of Mechanical and Nuclear Engineering, Pennsylvania State University, 227 Reber Building, University Park, PA 16802, USA
[b] Science and Technology Department, Westinghouse Electric Co., Pittsburgh PA, USA

ABSTRACT

The corrosion behavior and oxide structure of 9CrODS steel in supercritical water has been studied. Samples were exposed to supercritical water at 500 and 600 °C for times of 2, 4 and 6 weeks. The oxide structure was studied using microbeam synchrotron X-ray diffraction and fluorescence analysis. The 600 °C samples exhibited a three-layer structure with Fe_3O_4 in the outer layer, a mixture of $FeCr_2O_4$ and Fe_3O_4 in the inner layer, and a mixture of metal and oxide grains ($FeCr_2O_4$ and Cr_2O_3) in the diffusion layer. Between the 2 and 4-week samples exposed to 600 °C supercritical water, a Cr_2O_3 film appeared at the diffusion layer–metal interface which appears to be associated with slower oxidation of the metal. The 500 °C samples also showed a three-layer structure, but both the outer and inner oxide layers contained mainly Fe_3O_4, and the diffusion layer contained much fewer oxide precipitates and was a solid solution of oxygen ahead of the oxide front.

© 2009 Elsevier B.V. All rights reserved.

1. Introduction

As part of the Generation IV initiative, the supercritical water reactor (SCWR) design is considered for its high thermal efficiency and plant simplification. This reactor is designed to function above the critical point of water (374 °C and 22.1 MPa) at a temperature between 500 and 600 °C, and a pressure of 25 MPa [1]. Such high temperatures create a highly corrosive environment for the materials, and as a result, corrosion resistance becomes a key requirement for the candidate structural materials. The primary candidates for the supercritical water reactor design are ferritic-martensitic steels and oxide dispersion strengthened steels (ODS), such as the 9CrODS steel alloy which is discussed in this paper.

9CrODS steel is a ferritic-martensitic steel containing a fine dispersion of nano-particles of yttrium rich oxides in the alloy matrix. This alloy was developed by Japan Atomic Energy Agency for application in sodium cooled fast reactors [2,3]. It exhibits higher creep strength and radiation damage resistance than conventional ferritic-martensitic steels [2,3]. This alloy also exhibits good corrosion resistance, which has been suggested to be caused by the enhanced chromium segregation at the grain boundaries to form Cr_2O_3 [4,5].

In this study, 9CrODS steel was oxidized at two temperatures (500 and 600 °C) for three different times (2, 4 and 6 weeks). The oxide layers formed on these samples were characterized using microbeam synchrotron X-ray diffraction and fluorescence, and scanning electron microscopy (SEM). Preliminary results on the steel exposed at 600 °C for 4 weeks were described in a previous article [6]. This paper expands analysis of this alloy to include the influence of exposure time and temperature on the oxide microstructure.

2. Experimental procedures

The 9CrODS steel samples were supplied by Japan Atomic Energy Agency. The ODS Y_2O_3 particles were mechanically mixed with the other elements before being sealed in cans under vacuum of 0.1 Pa at 400 °C, and then hot-extruded and forged at 1150 °C. The alloy was normalized for one hour at 1050 °C, air-cooled, and then tempered at 800 °C for one hour. The details of the manufacturing process are described elsewhere [3]. The chemical composition of the alloy is shown in Table 1.

The corrosion experiments were performed in the natural circulation supercritical water corrosion loop at the University of Wisconsin. The supercritical loop is described in more detail in other articles [7,8]. The pressure was 25 MPa, the dissolved oxygen content was ~25 ppb, and the temperature and exposure time depended on the sample: 500 or 600 °C for 2, 4 or 6 weeks.

2.1. Sample preparation

The oxidized coupons were cut using a diamond saw to expose their cross-sections and create thin strips which were mounted into a slotted molybdenum rod inserted in a 3 mm round brass tube which was filled with a copper-based epoxy [9]. This method is used to protect the oxide scale during the sample preparation. It should be noted that the oxide adhered well to the metal and little edge loss was detected. Disk shaped cross sectional samples were

* Corresponding author. Tel.: +1 814 321 3474; fax: +1 814 865 8499.
E-mail address: jbb236@psu.edu (J. Bischoff).

Table 1
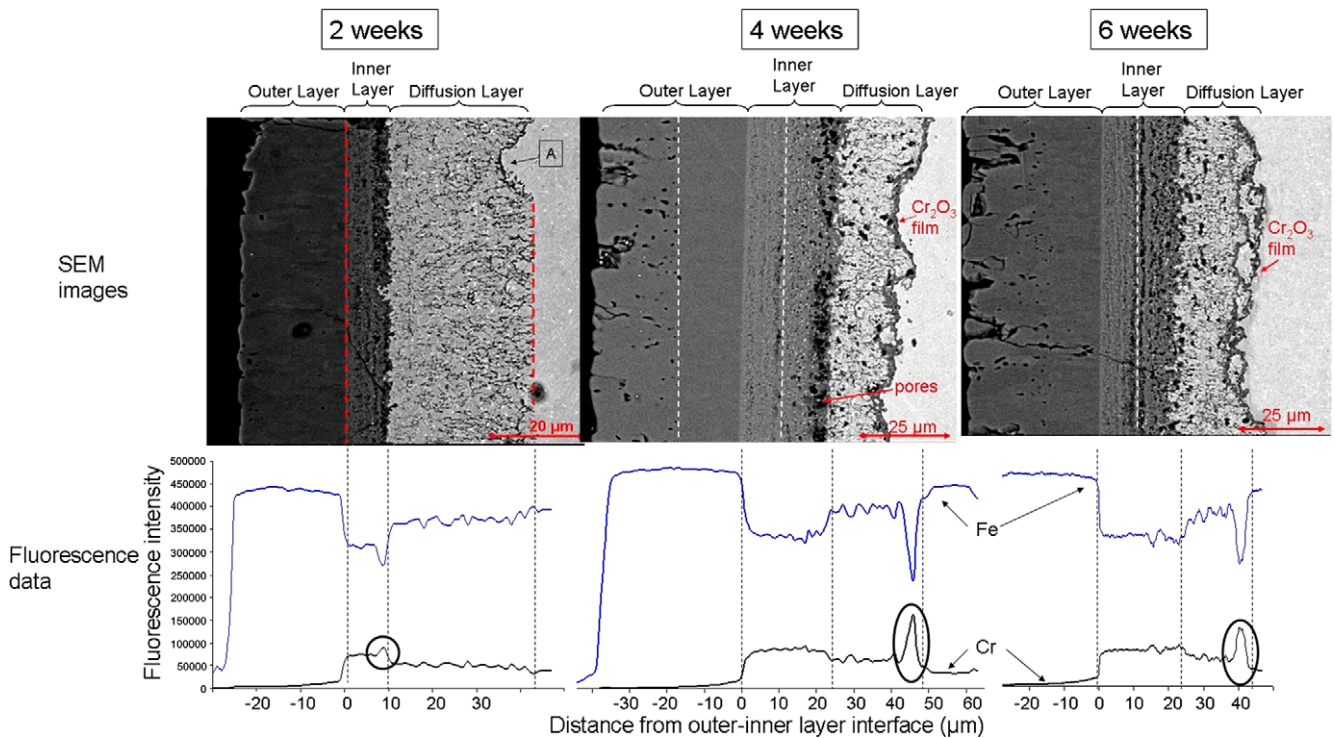Chemical composition of 9Cr ODS F/M steel (wt%, balance Fe).

Alloy	C	O	Si	P	S	Ti	Cr	Mn	Ni	Y	W
9Cr ODS	0.14	0.14	0.048	<0.05	0.003	0.21	8.6	0.05	0.06	0.28	2
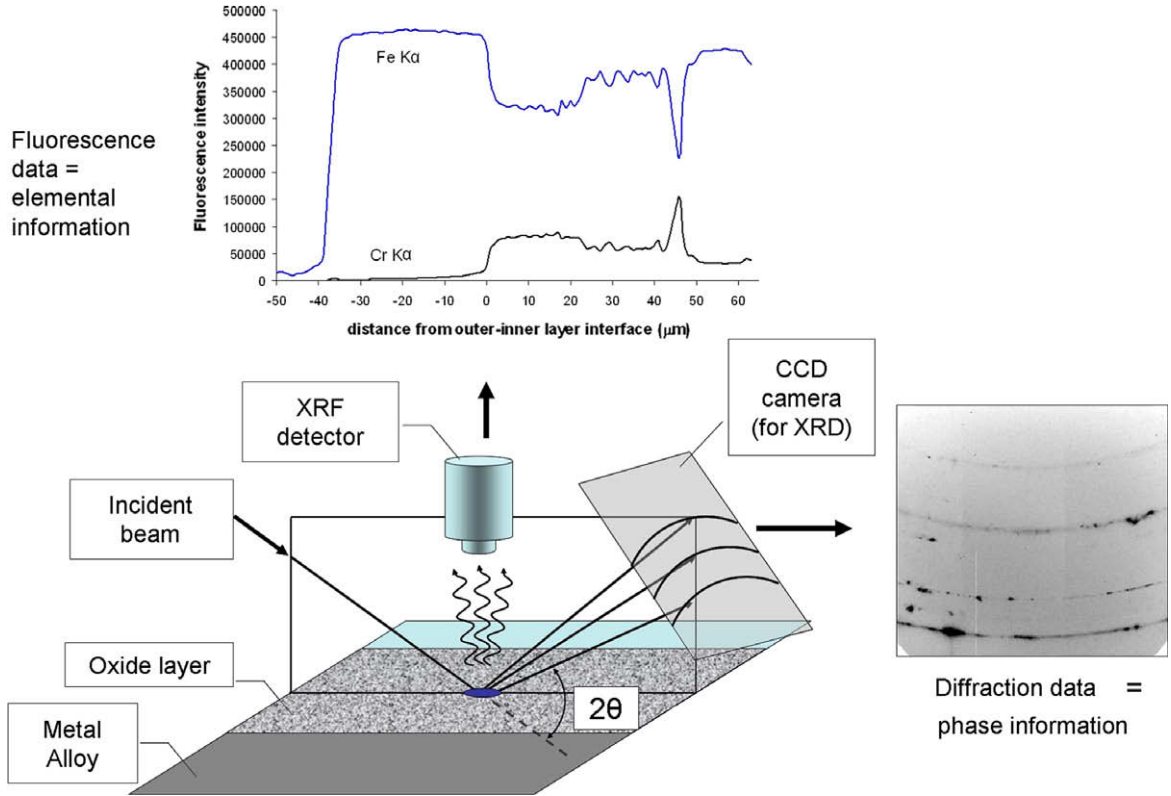
Fig. 1. Diffraction geometry and data acquisition at the 2-ID-D beamline at the APS facility in Argonne National Laboratory.

Fig. 2. SEM images and fluorescence data for the 600 °C 2, 4 and 6-week samples.
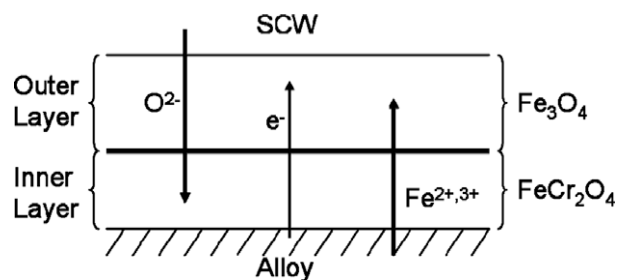
Fig. 3. Schematic of the oxidation mechanism in supercritical water.

sliced from the brass tube configuration. These samples were polished to a mirror finish with 1200 grit sandpaper followed by 1 μm diamond paste and finally a 0.05 μm colloidal silica solution. These samples were used for both the examination in the synchrotron radiation facility and the SEM analysis.

2.2. Microbeam synchrotron radiation diffraction and fluorescence

The synchrotron X-ray diffraction and fluorescence experiment was performed at the 2-ID-D beamline of the Advanced Photon Source at Argonne National Laboratory, in which the incident beam can be focused to a 0.2 μm spot at an energy of 9.5 keV. Fig. 1 shows the diffraction geometry at the beamline. The incident beam angle (16°) created a footprint on the sample of about 0.2×2 μm^2. Both diffraction and fluorescence information are acquired simultaneously for each spot. Consequently, the whole oxide layer was scanned spot by spot to obtain the diffraction peaks (which when indexed give a 'map' of the phases present) and elemental composition of the oxide.

The diffraction data were analyzed by manual fit of individual peaks using PeakFit [10] to determine the location and area of the peaks. In particular, this technique enabled differentiation between Fe_3O_4 and $FeCr_2O_4$, two phases that have the same crystal structure and similar cell parameters. With an energy of 9.5 keV, the 100% intensity peak associated with Fe_3O_4 is located at a diffraction angle of 29.87° (PDF# 19-0629) while that for $FeCr_2O_4$ is

located at an angle of 29.94° (PDF# 34-0140). For the indexing of Cr_2O_3 and FeO the powder diffraction files used were PDF# 38-1479 and PDF# 06-0615, respectively.

3. Results and discussion

3.1. Samples oxidized at 600 °C

Fig. 2 shows SEM images and fluorescence data for samples oxidized at 600 °C for 2, 4 and 6 weeks. The SEM images showed that all samples exhibited a three-layer oxide structure: outer, inner and diffusion layers. As observed previously, the outer oxide contained only Fe_3O_4, the inner oxide consisted of a mixture of Fe_3O_4 and $FeCr_2O_4$, and the diffusion layer contained a mixture of oxide precipitates ($FeCr_2O_4$) and iron bcc metal grains. Additionally, the SEM images of the inner layer showed periodic lines of pores suggesting some periodicity in the oxidation process.

In all samples, the outer–inner oxide interface was distinct and is thought to be the original metal–water interface [5]. This is in agreement with an overall oxidation mechanism of an outer oxide formed by outward diffusion of the iron cations (Fe^{2+}), and inner oxide formation by inward diffusion of oxygen anions (O^{2-}) [4,5]. Fig. 3 shows a schematic of this oxidation mechanism. Both the outer and the inner oxide of the 4 and 6-week samples shown in Fig. 2 were divided into two sub-layers, one porous and one nonporous. In the outer oxide, the porous sub-layer was observed near the coolant whereas in the inner oxide it was observed near the inner oxide–diffusion layer interface.

The fluorescence data in Fig. 2 show both the iron Kα (top line) and the Cr Kα lines (bottom line). The fluorescence plots clearly show the three layers. The outer layer contains only iron (and oxygen), while the inner layer is enriched in chromium compared to the base metal and the diffusion layer. The chromium content of the diffusion layer is intermediate to that of the metal and the inner layer. Additionally, a chromium enrichment peak (circled) is observed at the inner oxide–diffusion layer interface for the 2-week sample but at the diffusion layer–metal interface for both the 4 and 6-week samples.
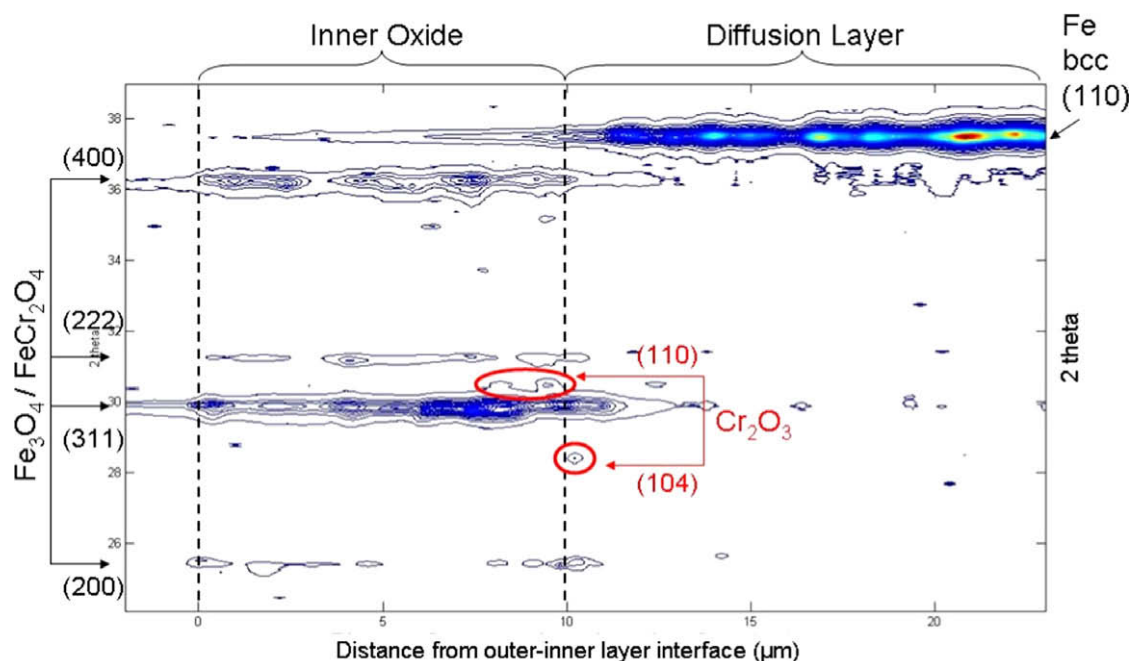

Fig. 4. Diffraction data of the inner and diffusion layers for the 600 °C 2-week sample acquired using a 0.2 μm step-size.

A major change occurs between 2 and 4 weeks with the formation of a relatively thick oxide film at the diffusion layer–metal interface. The beginning of the formation of this ribbon was observed in the SEM image of the 2-week sample in the region labeled 'A'. The fact that no oxide precipitates were observed in the base metal once this film formed suggests that this ribbon may have a significant role in the corrosion resistance of the 9CrODS steel. The formation of this film, between the 2 and 4-week samples, is accompanied by a shift of the chromium enrichment peak observed in the fluorescence data from the inner oxide–diffusion layer interface to the diffusion layer–metal interface. Consequently, the ribbon is formed by a chromium rich oxide which the diffraction data shows is Cr_2O_3.

The 600 °C 2-week sample had a diffusion layer three times larger than the inner layer, which suggests oxygen diffused deep into the alloy relatively fast. The diffusion layer ended at a uniform distance from the inner oxide–diffusion layer interface, which likely represents the location where the solubility limit of oxygen in the metal was exceeded. Oxide precipitates formed when the oxygen concentration was above that limit. The diffraction data for the 2-week sample shows that the outer layer was Fe_3O_4, the inner layer was a mixture of Fe_3O_4 and $FeCr_2O_4$, and the diffusion layer only contained $FeCr_2O_4$ and bcc-Fe. Diffraction peaks associated with the Cr_2O_3 phase were observed at the inner oxide–diffusion layer interface, where the fluorescence data showed chromium enrichment. The presence of Cr_2O_3 along with chromium enrich-
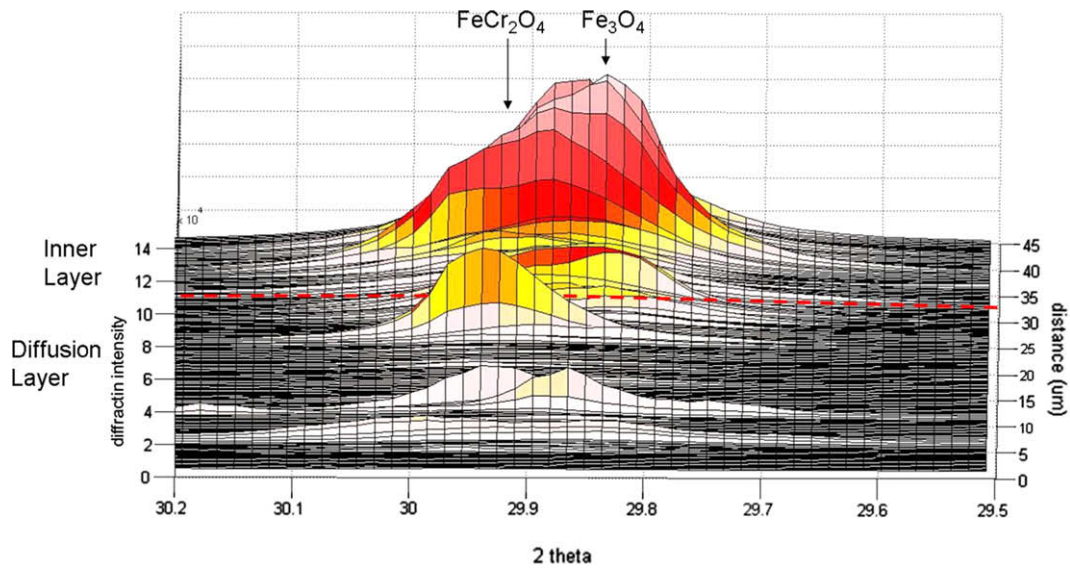

Fig. 5. Close-up of the diffraction data for the 600 °C 4-week sample on the peak associated with the (3 1 1) plane of both Fe_3O_4 and $FeCr_2O_4$.
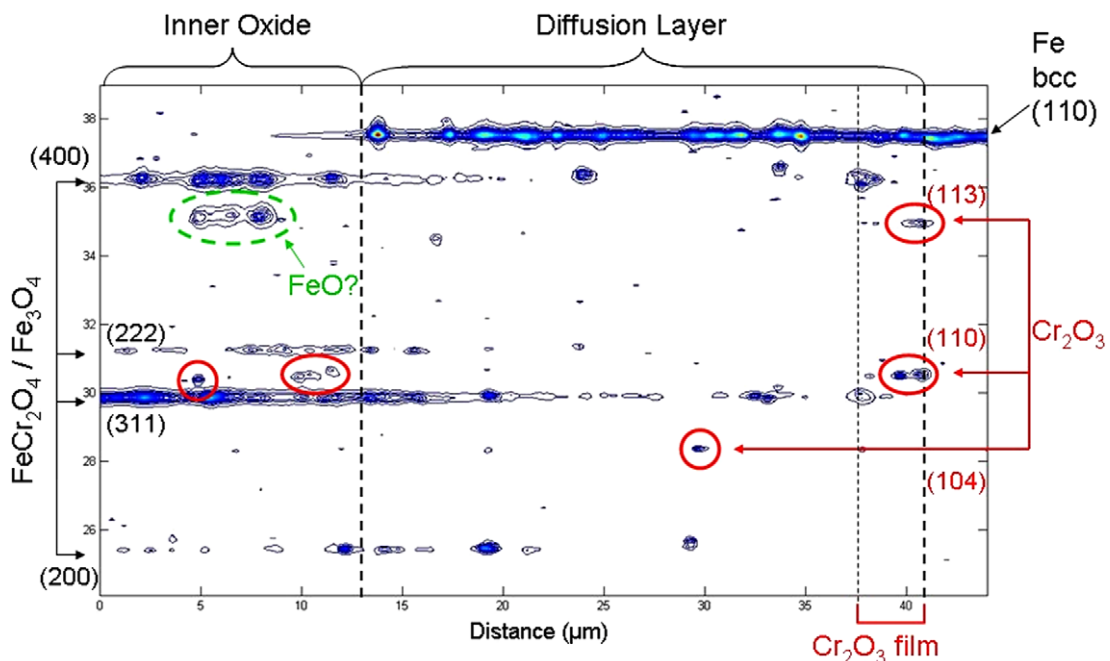

Fig. 6. Diffraction data for the 600 °C 4-week sample acquired using a step-size of 0.2 μm.

ment at the inner oxide–diffusion layer interface makes this interface play an active role in the corrosion resistance since Cr_2O_3 is known to hinder diffusion of oxygen and iron ions [11,12]. Fig. 4 shows the diffraction data for the 600 °C 2-week sample acquired with a 0.2 μm step-size.

The 600 °C 4-week sample showed a shift of the main peak associated with Fe_3O_4–$FeCr_2O_4$ from 29.94° ($FeCr_2O_4$) in the diffusion layer to 29.87° (Fe_3O_4) in the middle of the inner layer. Fig. 5 shows a close-up of the diffraction data on the peak associated with the Fe_3O_4–$FeCr_2O_4$ (3 1 1) plane where this shift is seen.

Fig. 6 shows the diffraction data for the 600 °C 4-week sample acquired using a 0.2 μm step-size. Apart from thicker oxide layers, the main difference between the 2-week and the 4-week samples was the presence of the continuous Cr_2O_3 ribbon. This ribbon was a few microns thick and is composed of both Cr_2O_3 and $FeCr_2O_4$. However, immediately next to the interface with the metal, the ribbon was a continuous layer of Cr_2O_3 with no $FeCr_2O_4$. Peaks associated with $FeCr_2O_4$ were observed in the region of the ribbon nearer to the diffusion layer. This phase layout is in agreement with thermodynamic data, since Cr_2O_3 forms at the lowest oxygen potential, followed by $FeCr_2O_4$ and then at higher oxygen potentials by Fe_3O_4 [13]. Fig. 7 shows the analysis of diffraction data ta-

ken in the Cr_2O_3 oxide film at the diffusion layer–metal interface. It is likely this continuous Cr_2O_3 present at the film–metal interface was responsible for slowing the diffusion of oxygen beyond the ribbon, thus inhibiting further oxidation of the metal [11]. Cr_2O_3 has been shown to serve both as a kinetic and thermodynamic oxidation barrier since the diffusion of species is slow through Cr_2O_3 but it also decreases the oxygen potential on the inner interface, thus hindering oxidation of the metal [12]. Additionally, a TEM investigation confirmed the presence of this Cr_2O_3 ribbon [14].

Furthermore, in Fig. 6, diffraction peaks associated with Cr_2O_3 (full circles) were observed at the inner oxide–diffusion layer interface. Since Cr_2O_3 hinders the diffusion of oxygen, this may explain the slow advancement of the inner oxide in the diffusion layer. Additionally, a large peak (circled with dotted line and labeled FeO) was observed in the inner oxide at a diffraction angle of about 35.2°. This peak is identified as the FeO (2 0 0) plane which diffracts at an angle of 35.29°.

The 600 °C 6-week sample appeared to be similar to the 4-week sample, in particular because of the presence of the Cr_2O_3 film. However, the microstructure of this sample differed from the 4-week sample. First, almost no $FeCr_2O_4$ was observed and Fe_3O_4 was present throughout the oxide layers including the diffusion
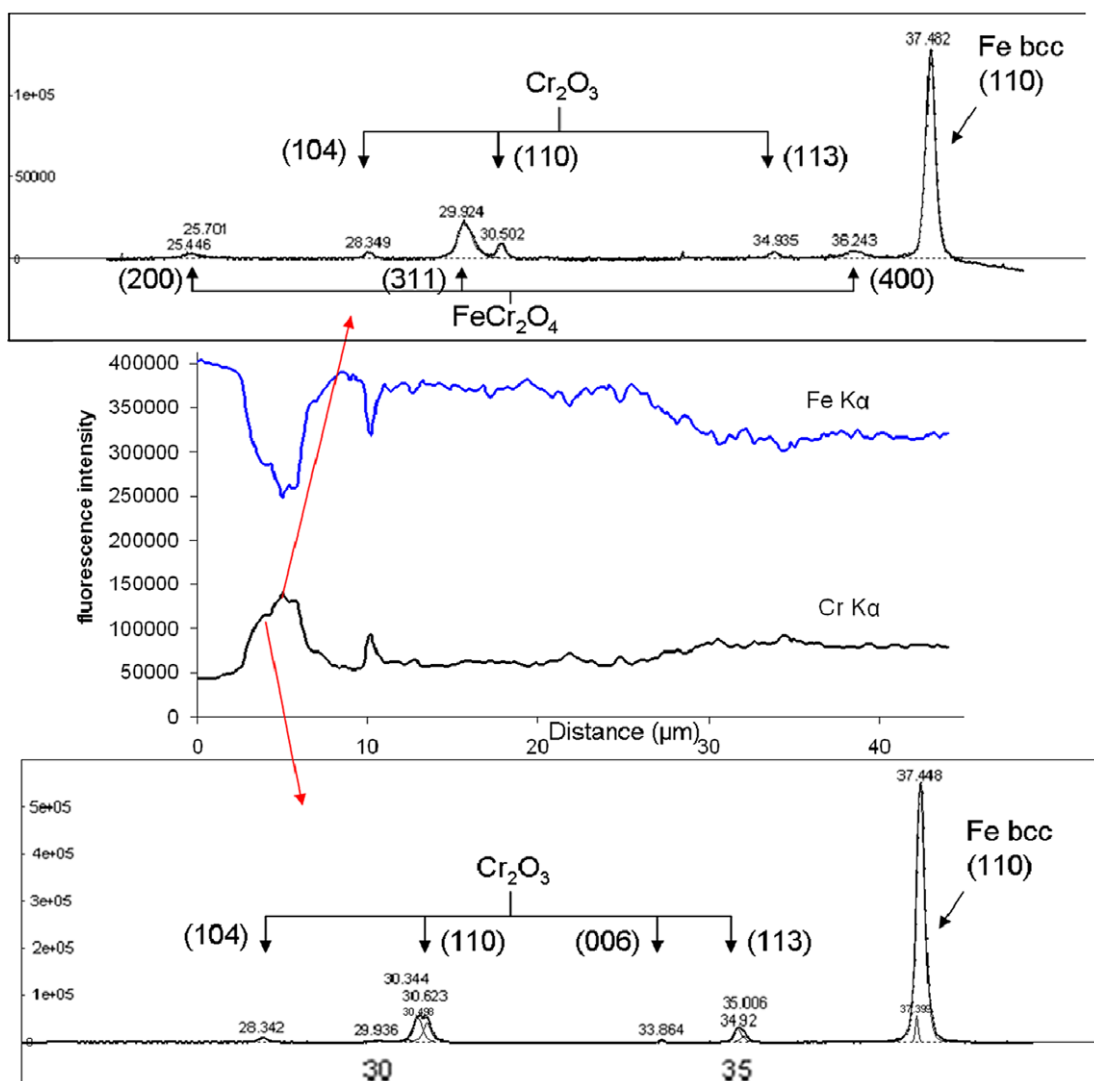

Fig. 7. Detailed PeakFit analysis of the oxide film at the diffusion layer–metal interface.
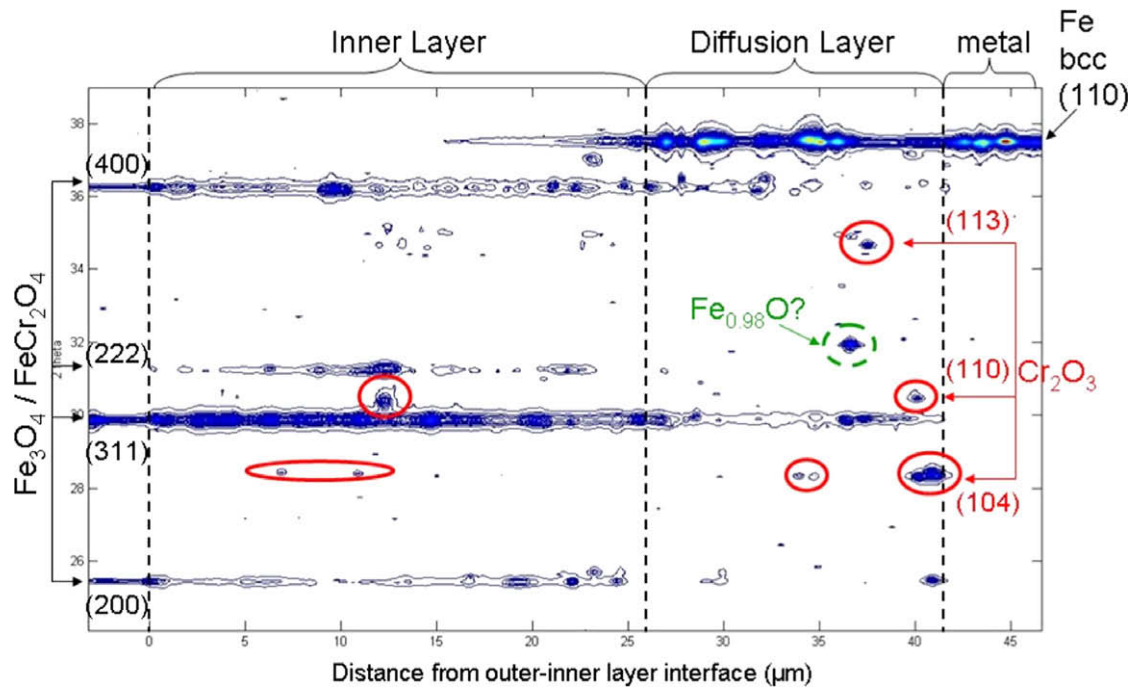
Fig. 8. Diffraction data for the 600 °C 6-week sample acquired using a 0.2 µm step-size.

layer. Fig. 8 shows the diffraction data for the 600 °C 6-week sample.

In the 6-week sample, the Cr_2O_3 present for shorter exposure times at the inner oxide–diffusion layer had disappeared, which could also explain the disappearance of the line of pores observed at that interface in the 2 and 4-week samples. The 6-week sample showed a non-linear inner oxide–diffusion layer interface and a greater interpenetration of the inner oxide into the diffusion layer (observed on the SEM image) suggesting advancement of the inner oxide into the diffusion layer. This is thought to be linked with the absence of Cr_2O_3 at this, causing a greater interpenetration of the inner oxide and the diffusion layer (observed on the SEM image), and moderate growth of the inner oxide.

Additionally, a strong peak at an angle of 31.9° (circled with dotted line and labeled $Fe_{0.98}O$ in Fig. 8 was observed right before the Cr_2O_3 ribbon in the diffusion layer. This peak may possibly be associated with the (1 0 1) plane of $Fe_{0.98}O$ normally located at 31.88°. Moreover, a remnant of the possible FeO peak that was observed in the 4-week sample was seen in the middle of the inner oxide.

3.2. Samples oxidized at 500 °C

Three samples were oxidized at 500 °C for the same exposure times as for the 600 °C samples: 2, 4 and 6 weeks. Only the 4 and 6-week samples were characterized using microbeam synchrotron radiation diffraction and fluorescence. Fig. 9 shows the SEM images of the three samples.

The oxide layers formed at 500 °C were different from the samples oxidized at 600 °C in several aspects. First, the oxide layers were much thinner. Whereas the outer layer thickness for the 600 °C 4-week sample was about 38 µm, it was only 6.5 µm for the 500 °C 4-week sample. Consequently, the oxidation is significantly slower at 500 °C. The structure of the diffusion layer–metal interface on the 6-week sample in Fig. 9 suggested that the diffusion of oxygen into the metal occurred by a grain boundary process, since oxides preferentially precipitated at the metal grain boundaries. In the 600 °C samples the oxide precipitates in the diffusion layer had not seemed to be formed by a grain boundary process since they had not outlined the metal grains.
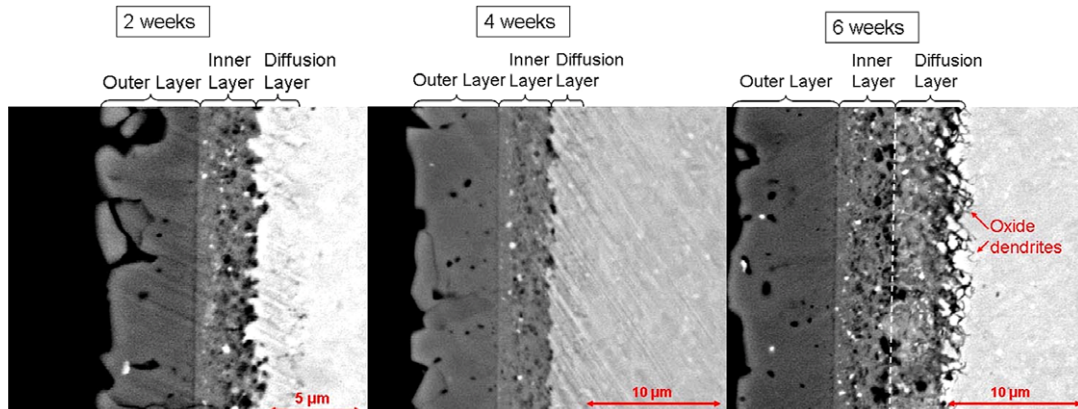

Fig. 9. SEM images for 9CrODS steel exposed to 500 °C supercritical water for 2, 4 and 6 weeks.
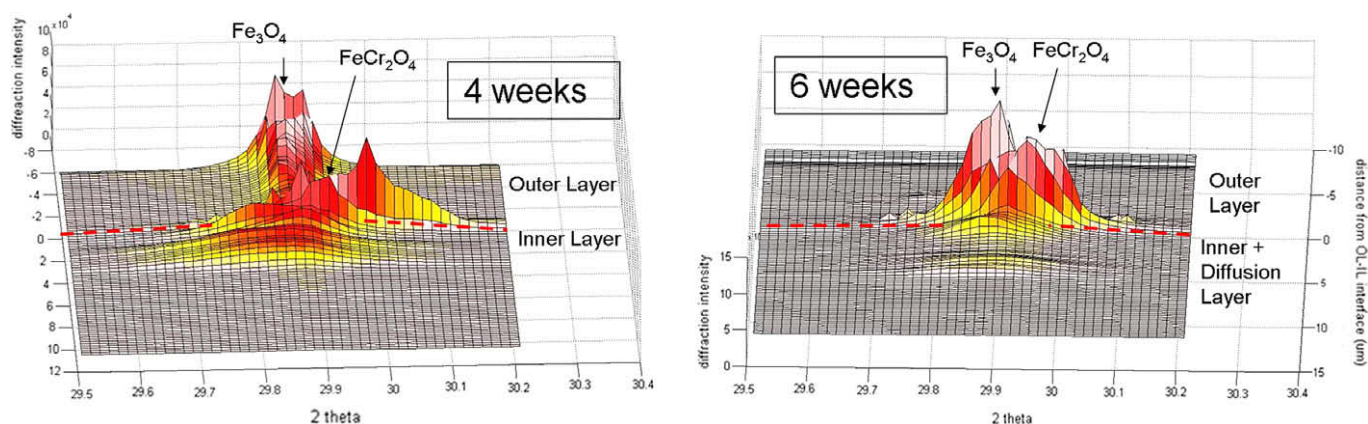
Fig. 10. Close up of the diffraction data centered on the 29.9° peak for the 500 °C 4 and 6-week samples.

Second, no distinct diffusion layer similar to that seen in the 600 °C samples was observed. A slight difference in contrast (the diffusion layer appeared darker than the metal) shows the presence of a diffusion layer. The 500 °C 6-week sample was different from the two other 500 °C samples in that respect, since its diffusion layer appeared similar to its inner oxide except with slightly lighter contrast. Nevertheless, the diffraction data showed very few oxide peaks in the diffusion layer of all the samples. This suggested that the diffusion layer in the 500 °C samples was a solid solution of oxygen containing few oxide precipitates.

Finally, the diffraction data showed that the main oxide phase formed throughout the oxide layers was Fe_3O_4. $FeCr_2O_4$ appeared mainly at the outer–inner oxide interface. Fig. 10 shows a close-up of the diffraction data on the main peak associated with Fe_3O_4–$FeCr_2O_4$ showing the presence of $FeCr_2O_4$ at the outer–inner oxide interface. Little Cr_2O_3 was observed, but a few peaks associated with that phase were seen both in the middle of the inner oxide and in the diffusion layer near the diffusion layer–metal interface. No chromium enrichment was observed in the fluorescence data at the locations where Cr_2O_3 was observed. Consequently, it appears that insufficient Cr_2O_3 formed (due to a low diffusion coefficient of chromium at 500 °C) to be able to serve as a barrier for oxidation, in contrast to the 600 °C samples. Several studies have shown that chromium diffuses much slower in ferritic steel at 500 than at 600 °C, by about two orders of magnitude (about $8 \times 10^{-20} \, m^2 \, s^{-1}$ at 600 °C and $3.5 \times 10^{-22} \, m^2 \, s^{-1}$ at 500 °C) [15,16]. Thus, it is possible that at 500 °C the diffusion of chromium in ferritic steel is too slow to form Cr_2O_3.

4. Conclusion

The oxide structure formed on 9CrODS steel exposed to supercritical water was characterized using microbeam synchrotron X-ray diffraction and fluorescence. Samples were oxidized at temperatures of 500 and 600 °C for exposure times of 2, 4 and 6 weeks.

The main conclusions are:

1. 9CrODS steel formed a three-layer oxide structure. For the 600 °C samples, the outer layer contained Fe_3O_4, the inner oxide contained a mixture of $FeCr_2O_4$ and Fe_3O_4, and the diffusion layer contained a mixture of $FeCr_2O_4$ precipitates and base metal grains. For the 500 °C samples, the outer and inner layers both contained Fe_3O_4, and the diffusion layer was a solid solution of oxygen containing few precipitates.

2. The corrosion mechanism appeared to be the outward diffusion of iron ions produced by the oxidation of the metal, which served to form the outer layer, while the inward diffusion of oxygen formed the inner oxide.

3. In the samples exposed at 600 °C, a Cr_2O_3 film formed at the diffusion layer–metal interface between the 2 and 4-week samples. This continuous layer of Cr_2O_3 appeared to stop or dramatically slow down the diffusion of oxygen beyond the film and thus served as a barrier for further oxidation.

4. Chromium enrichment associated with the presence of Cr_2O_3 is observed at the inner oxide–diffusion layer interface for the 600 °C 2-week sample, and at the diffusion layer–metal interface for the 600 °C 4 and 6-week samples.

5. It is not yet possible to know if this material is suitable for application in a Supercritical Water Reactor. Further experiments concerning the stability of the ODS particles and their role in the corrosion resistance still have to be investigated, and this material should be compared to non-ODS ferritic-martensitic steels.

Acknowledgements

References

[1] A Technology Roadmap for Generation IV Nuclear Energy Systems, US DOE NERAC and Generation IV International Forum GIF-002-00, 2002.
[2] S. Ohtuska, S. Ukai, M. Fujiwara, T. Kaito, T. Narita, Mater. Trans. 46 (2005) 1.
[3] S. Ukai, S. Mizuta, T. Yoshitake, T. Okuda, M. Fujiwara, S. Hagi, T. Kobayashi, J. Nucl. Mater. 283–287 (2000) 702.
[4] Y. Chen, K. Sridharan, T.R. Allen, S. Ukai, J. Nucl. Mater. 359 (2006) 50.
[5] Y. Chen, K. Sridharan, S. Ukai, T.R. Allen, J. Nucl. Mater. 371 (2007) 118.
[6] A.T. Motta, A.D. Siwy, J.M. Kunkle, J.B. Bischoff, R.J. Comstock, Y. Chen, T.R. Allen, Proceedings of 13th NACE International Conference on Environmental Degradation of Materials in Nuclear Power Plants, 2007.
[7] K. Sridharan, S.P. Harrington, A.K. Johnson, J.R. Licht, M.H. Anderson, T.R. Allen, Mater. Design 28 (2007) 1177.
[8] K. Sridharan, A. Zillmer, J.R. Licht, T.R. Allen, M.H. Anderson, L. Tan, Proceedings of International Conference on Advances on Power Plants, Pittsburgh, PA, 2004.

[9] A. Yilmazbayhan, A.T. Motta, R.J. Comstock, G.P. Sabol, B. Lai, Z. Cai, J. Nucl. Mater. 324 (2004) 6.

[10] PeakFit, 4.0 Software for Windows ed: SPSS Chicago, IL, USA, 1997.

[11] Y. Ishikawa, T. Yoshimura, M. Arai, Vacuum 47 (1996) 701.

[12] A.C.S. Sabioni, A.M. Huntz, F. Silva, F. Jomard, Mater. Sci. Eng. A 392 (2005) 254.

[13] L. Tan, Y. Yang, T.R. Allen, Corros. Sci. 48 (2006) 3123.

[14] A.D. Siwy, T.E. Clark, A.T. Motta, J. Nucl. Mater., accepted for publication.

[15] J. Cermák, J. Ruzicková, A. Pokorná, Scr. Mater. 35 (1996) 411.

[16] Z. Tokei, K. Hennesen, H. Viefhaus, H.J. Grabke, Mater. Sci. Technol. 16 (2000) 1129.